Article

Strongly Birefringent PbOCl Nanobelts

Michael B. Sigman, and Brian A. Korgel
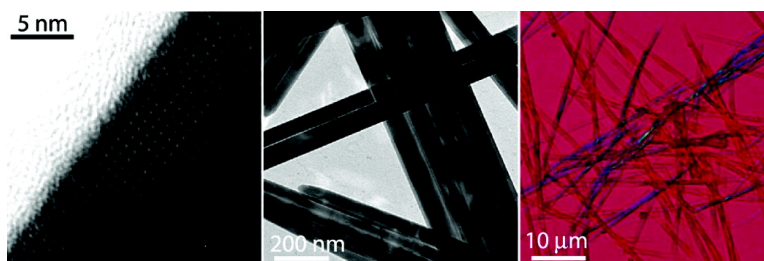
More About This Article

Additional resources and features associated with this article are available within the HTML version:

- Supporting Information
- Links to the 9 articles that cite this article, as of the time of this article download
- Access to high resolution figures
- Links to articles and content related to this article
- Copyright permission to reproduce figures and/or text from this article

View the Full Text HTML

Strongly Birefringent Pb₃O₂Cl₂ Nanobelts

Michael B. Sigman, Jr. and Brian A. Korgel*

Contribution from the Department of Chemical Engineering, Texas Materials Institute, Center for Nano- and Molecular Science and Technology, The University of Texas at Austin, Austin, Texas 78712-1062

Received March 27, 2005; E-mail: korgel@che.utexas.edu

Abstract: Orthorhombic $Pb_3O_2Cl_2$ (mendipite) nanobelts micrometers in length and tens of nanometers wide were synthesized by a solventless thermolysis of a single-source precursor in the presence of capping ligands. The nanobelts are single crystals elongated preferentially in the [010] direction. $Pb_3O_2Cl_2$ is a birefringent material due to its anisotropic crystal structure. The nanobelts exhibit birefringence enhanced by 1 order of magnitude as a result of their small size and belt geometry exceeding the birefringence of naturally occurring minerals, including $CaCO_3$ and TiO_2. The preferential elongation of the nanobelts in the [010] direction contributes to this enhancement.

Introduction

Materials with anisotropic crystal structure exhibit a variety of physical properties that depend strongly on crystallographic direction, such as the refractive index (i.e., birefringent materials),[1-4] the permanent dipole moment in ferroelectrics,[5-7] the magnetocrystalline anisotropy in ferromagnets,[8,9] and carrier mobilities in ionic conductors.[10-13] In nanomaterials, this orientational dependence can be enhanced by producing nanorods and nanowires elongated along a preferred crystal axis.[14,15] The effects of shape anisotropy in magnetic materials are relatively well-known;[16,17] however, the effects of controlled shape with preferred and uniform crystallographic orientation are relatively unexplored for most other classes of nanomaterials due to the lack of synthetic capability.

In recent years, colloidal synthetic routes have been developed for nanorods and nanowires, such as shape-directed arrested precipitation using surfactants that selectively adsorb to specific lattice planes,[18-21] metal particle-seeded solution-liquid–solid (SLS) growth,[21-25] controlled particle coagulation,[26,27] controlled epitaxial colloidal deposition,[28,29] and templating with porous alumina membranes to direct growth.[30] Recent studies have shown that anisotropic crystal structure provides a very strong driving force for aspherical colloid growth, with the nanocrystal morphology or habit often reflecting the underlying crystal structure and exhibiting a preferred crystallographic orientation.[31-33] In solventless routes using single-source precursors with capping ligands, the influence of the crystal structure has been particularly pronounced, leading to nanoscale crystallites with shapes and crystallographic orientations that directly mirror the internal crystal structure of the material, including Cu_2S (hexagonal) nanodisks,[34,35] NiS (rhombohedral) nanorods (and nanoprisms),[36] and Bi_2S_3 (orthorhombic) nanowires.[37] Capping

(1) Heer, W. A. d.; Bacsa, W. S.; Châtelain, A.; Gerfin, T.; Humphrey-Baker, R.; Forro, L.; Ugarte, D. *Science* **1995**, *268*, 845−847.
(2) Lemaire, B. J.; Davidson, P.; Ferré, J.; Jamet, J. P.; Panine, P.; Dozov, I.; Jolivet, J. P. *Phys. Rev. Lett.* **2002**, *88*, 125507/1−4.
(3) Kovalev, D.; Polisski, G.; Diener, J.; Heckler, H.; Künzner, N.; Timoshenko, V. Y.; Koch, F. *Appl. Phys. Lett*. **2001**, *78*, 916−918.
(4) Hartshorne, N. H.; Stuart, A. *Crystals and the Polarising Microscope*; Edward Arnold Ltd.: London, 1960.
(5) Sasaki, T.; Katsuragi, A.; Mochizuki, O.; Nakazawa, Y. *J. Phys. Chem. B* **2003**, *107*, 7659−7665.
(6) Glinchuk, M. D.; Morozovskaya, A. N. *Phys. Status Solidi B* **2003**, *238*, 81−91.
(7) Kim, H.-W.; Lee, H.-S.; Kim, J.-D. *Liq. Cryst.* **2002**, *29*, 413−420.
(8) Diehl, M. R.; Yu, J.-Y.; Heath, J. R.; Held, G. A.; Doyle, H.; Sun, S.; Murray, C. B. *J. Phys. Chem. B* **2001**, *105*, 7913−7919.
(9) Jun, Y.-W.; Jung, Y.-Y.; Cheon, J. *J. Am. Chem. Soc.* **2002**, *124*, 615−619.
(10) Nassary, M. M.; Gerges, M. K.; Shaban, H. T.; Salwa, A. S. *Physica B* **2003**, *337*, 130−137.
(11) Hasenöhrl, S.; Novák, J.; Kúdela, R.; Betko, J.; Morvic, M.; Fedor, J. *J. Cryst. Growth* **2003**, *248*, 369−374.
(12) Niitsu, G. T.; Nagata, H.; Rodrigues, A. C. *J. Appl. Phys.* **2004**, *95*, 3116−3119.
(13) Rodrigues, V.; Fuhrer, T.; Ugarte, D. *Phys. Rev. Lett.* **2000**, *85*, 4124−4127.
(14) Xia, Y.; Yang, P.; Sun, Y.; Wu, Y.; Mayers, B.; Gates, B.; Yin, Y.; Kim, F.; Yan, H. *Adv. Mater.* **2003**, *15*, 353−389.
(15) Law, M.; Goldberger, J.; Yang, P. *Annu. Rev. Mater. Res.* **2004**, *34*, 83−122.
(16) Park, S.-J.; Kim, S.; Lee, S.; Khim, Z. G.; Char, K.; Hyeon, T. *J. Am. Chem. Soc.* **2000**, *122*, 8581−8582.
(17) Park, J. I.; Kang, N. J.; Jun, Y. W.; Oh, S. J.; Ri, H. C.; Cheon, J. *ChemPhysChem* **2002**, *6*, 543−547.

(18) Peng, X.; Manna, U.; Yang, W.; Wickham, J.; Scher, E.; Kadavanich, A.; Allvisatos, A. P. *Nature* **2000**, *404*, 59−61.
(19) Puntes, V. F.; Zanchet, D.; Erdonmez, C. K.; Alivisatos, A. P. *J. Am. Chem. Soc.* **2002**, *124*, 12874−12880.
(20) Gates, B.; Mayers, B.; Cattle, B.; Xia, Y. *Adv. Funct. Mater.* **2002**, *12*, 219−227.
(21) Qian, C.; Kim, F.; Ma, L.; Tsui, F.; Yang, P.; Liu, J. *J. Am. Chem. Soc.* **2004**, *126*, 1195−1198.
(22) Holmes, J. D.; Johnston, K. P.; Doty, R. C.; Korgel, B. A. *Science* **2000**, *287*, 1471−1473.
(23) Yu, H.; Buhro, W. E. *Adv. Mater.* **2003**, *15*, 416−419.
(24) Kan, S.; Mokari, T.; Rothenberg, E.; Banin, U. *Nat. Mater.* **2003**, *2*, 155−158.
(25) Grebinski, J. W.; Hull, K. L.; Zhang, J.; Kosel, T. H.; Kuno, M. *Chem. Mater.* **2004**, *16*, 5260−5272.
(26) Tang, Z. Y.; Kotov, N. A.; Giersig, M. *Science* **2002**, *297*, 237−240.
(27) Lu, W.; Gao, P.; Jian, W. B.; Wang, Z. L.; Fang, J. *J. Am. Chem. Soc.* **2004**, *126*, 14816−14821.
(28) Milliron, D. J.; Hughes, S. M.; Cui, Y.; Manna, L.; Li, J.; Wang, L.-W.; Alivisatos, A. P. *Nature* **2004**, *430*, 190−195.
(29) Kudera, S.; Carbone, L.; Casula, M. F.; Cingolani, R.; Falqui, A.; Snoeck, E.; Parak, W. J.; Manna, L. *Nano Lett.* **2005**, *5*, 445−449.
(30) Pena, D.; Mbindyo, J.; Carado, A.; Mallouk, T.; Keating, C.; Razavi, B.; Mayer, T. *J. Phys. Chem. B* **2002**, *106*, 7458−7462.
(31) Gates, B.; Yin, Y.; Xia, Y. *J. Am. Chem. Soc.* **2000**, *122*, 12582−12583.
(32) Lee, S.-M.; Cho, S.-N.; Cheon, J. *Adv. Mater.* **2003**, *15*, 441−444.
(33) Mayers, B.; Xia, Y. *J. Mater. Chem.* **2002**, *12*, 1875−1881.

ligands in the solventless reaction mixture moderate the crystallization kinetics to prevent particle aggregation and maintain narrow size- and shape distributions, but the internal crystal structure tends to determine the nanocrystal shape.

Here, we report the solventless synthesis of [010]-oriented orthorhombic $Pb_3O_2Cl_2$ (mendipite) nanobelts. The nanobelt morphology and preferred crystallographic orientation imitate the bulk $Pb_3O_2Cl_2$ crystal structure. $Pb_3O_2Cl_2$ is a birefringent mineral with a birefringence of 0.07 due to its anisotropic crystal structure. In a bulk crystal, its slow optical axis is in the [010] direction. Due in part to the preferrential elongation of the nanobelts in the [010] crystallographic direction, along with the nanometer-scale diameter and anisotropic shape, the nanobelts exhibit strongly enhanced birefringence relative to the bulk material, enhanced by more than 1 order of magnitude. Three different optical polarization microscopy methods were used to determine the birefringence: interference colors using the Michel Lévy chart, Bräce−Köhler compensation, and de Sénarmont compensation. The birefringence is found to be ∼1.1, which is significantly higher than the birefringence of naturally occurring minerals, including $CaCO_3$ (0.154) and TiO_2 (0.287).[38]

Experimental Details

$Pb_3O_2Cl_2$ Nanobelt Synthesis. All chemicals were used as supplied from Aldrich Chemical Co. Water was doubly distilled and deionized (DI). $Pb_3O_2Cl_2$ nanobelts were obtained by thermolysis of a lead chloride ($PbCl^+$) octanoate complex in the absence of solvent, similar to previous work for Cu_2S, NiS, and Bi_2S_3.[34,36,37] Lead (II) chloride ($PbCl_2$, 0.20 g) is added to 32 mL of DI-H_2O and briefly sonicated to form a slightly cloudy dispersion. Chloroform ($CHCl_3$, 25 mL) with 0.17 g of sodium octanoate ($NaOOC(CH_2)_6CH_3$) is added to the aqueous solution to form a two-phase mixture. $PbCl_2$ dissociates to $PbCl^+$ in water,[39] which complexes with sodium octanoate and transfers into the organic phase. The mixture is stirred for 20 min and separated, the aqueous phase discarded. Ethylenediamine ($C_2H_8N_2$, 500 μL) is added to the organic solution and stirred for 10 min. Ethylenediamine inhibits particulate growth and improves the nanobelt yield (see Supporting Information). Evaporation of organic solvent on a rotary evaporator gives an opaque grayish-white solid, which serves as the nanobelt precursor.

Heating the precursor in air for 1 h at 190 °C leads to O−C thermolysis of the PbCl−octanoate complex and generates a gray solid. The gray solid is an impure mixture of nanobelts and reaction byproducts. The nanobelts are purified by redispersion in chloroform with mild sonication followed by precipitation with ethanol. The precipitate is isolated by brief centrifugation at 4000 rpm for 5 min. The supernatant is discarded to yield purified nanobelts, which appear as a white powder. The reaction yield is 30%.

Nanobelt Characterization. The nanobelts were characterized by transmission electron microscopy (TEM), X-ray diffraction (XRD), electron diffraction (ED), scanning electron microscopy (SEM), and optical polarization microscopy.

High-resolution TEM and ED were performed on a JEOL 2010F TEM equipped with a field emission gun operating at 200 kV accelerating voltage. Images were acquired digitally on a Gatan multipole scanning CCD camera. Lower-resolution TEM images were

obtained using a Philips 208 TEM with 80 kV accelerating voltage. TEM samples were prepared by drop casting from chloroform onto 200 mesh lacey carbon-coated Cu grids (Electron Microscopy Sciences). ED patterns were simulated with the JEMS software package using cell dimensions of 11.879 Å × 5.809 Å × 9.511 Å for the orthorhombic mendipite structure and Pb, O, and Cl atomic positions as determined by Krivovichev and Burns[40] and Norén et al.[41]

SEM was performed on a LEO 1530 field emission gun SEM operating at 1 kV accelerating voltage with digital image acquisition using an Inlens detector and LEO 32 software system. SEM samples were prepared by drop casting from chloroform onto glassy carbon substrates approximately 1 cm × 1 cm and 1 mm thick.

XRD was performed using a Bruker-Nonius D8 Advance Theta-2Theta powder diffractometer with Cu Kα radiation ($\lambda = 1.54$ Å) and a Bruker Sol-X Si(Li) solid-state detector. For XRD, nanobelts were drop cast (∼5 mg) from chloroform onto a quartz (001) substrate and then scanned for 8 h at a 0.02° angle increment with samples rotating at 12°/min.

Optical polarization microscopy was performed on a Carl Zeiss Axioskop 2MAT microscope equipped with a 40× plan-NEOFLUAR polarizing objective lens with 0.85 numerical aperture, a 50× EC Epiplan-NEOFLUAR objective lens with 0.8 numerical aperture, a 100× EC Epiplan-NEOFLUAR objective lens with 0.9 numerical aperture, polarization filters, and a halogen light source. Imaging and optical path differences (OPD) were measured in transmission mode under Köhler illumination with digital image acquisition using an AxioCam MRc5 CCD camera. The nanobelt optical path differences were determined using three separate techniques: interference colors, Bräce−Köhler compensation, and de Sénarmont compensation. A Carl-Zeiss Red 1 filter with a 550 nm OPD was used to induce interference colors suitable for use of a Michel Lévy chart. de Sénarmont measurements were made using a de Sénarmont compensator consisting of an Olympus quarter wave plate (U-P540), a 546 nm narrow band filter (9-U150), and the 180° rotating analyzer on the microscope. Bräce−Köhler measurements were performed on a Carl Zeiss Ultrapolariscope III with λ/20 compensator using either a 546 or a 656 nm band-pass filter.

Nanobelt thickness was determined using a Digital Instruments Dimension 3100 atomic force microscope (AFM) operating in tapping mode. Images were acquired using PPP-NCL noncontact/tapping mode cantilevers from Nanosensors with a tip radius of curvature of <10 nm, force constant of 42 N/m, and resonant frequency of 330 kHz.

Results and Discussion

Nanobelt Structure and Crystallographic Details. The solventless synthesis yields nanobelts of orthorhombic Pb_3O_2-Cl_2 (mendipite). Panels A−G in Figure 1 show TEM and SEM images and Figure 1H shows the XRD pattern. The nanobelts align into bundles with individual nanobelts being greater than 4 μm long, often extending up to 20 μm. The nanobelt widths range from 29 to 170 nm with a log-normal average of 61.6 nm, and the thickness fits a normal distribution with an average value of 23.3 nm ($\sigma = \pm 26\%$) (see Supporting Information). In the XRD patterns, the (200) and (600) peak intensities are enhanced, the (020) and (013) peak intensities are decreased, and the (211), (112), (311), (113), and (033) reflections are absent, relative to bulk mendipite. The differences in peak intensity result from the preferred crystallographic orientation of the nanobelts. The [010] growth direction was observed by TEM in 90% of the nanobelts (18 of 20 nanobelts examined). A [013] growth direction was observed in the remaining 10%

(34) Larsen, T. H.; Sigman, M.; Ghezelbash, A.; Doty, R. C.; Korgel, B. A. *J. Am. Chem. Soc.* **2003**, *125*, 5638−5639.
(35) Sigman, M. B.; Ghezelbash, A.; Hanrath, T.; Saunders: A. E.; Lee, F.; Korgel, B. A. *J. Am. Chem. Soc.* **2003**, *125*, 16050−16057.
(36) Ghezelbash, A.; Sigman, M. B.; Korgel, B. A. *Nano Lett.* **2004**, *4*, 537−542.
(37) Sigman, M. B.; Korgel, B. A. *Chem. Mater.* **2005**, *17*, 1655−1660.
(38) Hecht, E. *Optics*, 3rd ed.; Addison-Wesley: New York, 1998.
(39) Cotton, F. A.; Wilkinson, G. *Advanced Inorganic Chemistry*, 3rd ed.; John Wiley & Sons: New York, 1972.

(40) Krivovichev, S. V.; Burns, P. C. *Eur. J. Mineral.* **2001**, *13*, 801−809.
(41) Noren, L.; Tan, E. S. Q.; Withers, R. L.; Sterns, M.; Rundlof, H. *Mater. Res. Bull.* **2002**, *37*, 1431−1442.
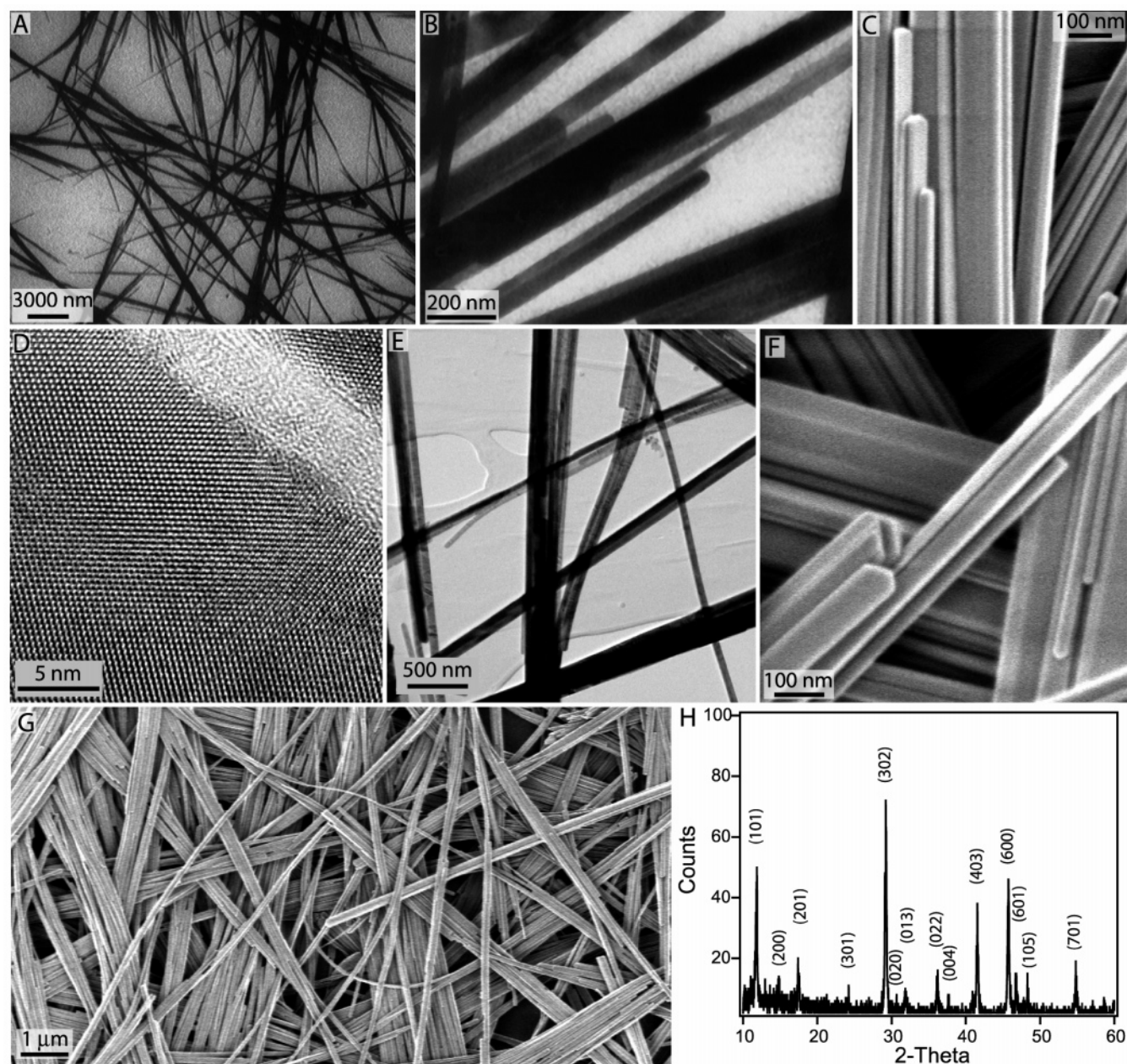
Figure 1. (A,B,D,E) TEM images of highly crystalline Pb$_3$O$_2$Cl$_2$ nanobelts formed via the solventless thermolysis technique. (C,F,G) SEM images of Pb$_3$O$_2$Cl$_2$ nanobelts. (H) XRD pattern of the nanobelts matches orthorhombic Pb$_3$O$_2$Cl$_2$ (mendipite) (JCPDS PDF number 25-0448).

of the wires. Both crystallographic orientations are consistent with rectangular prism or belt-like morphology.

Figure 2 shows HRTEM images and ED patterns obtained from two nanobelts with different crystallographic orientations: [010] (Figure 2A) and [013] (Figure 2D). The nanobelts in Figure 2 are imaged with the beam penetrating the belt thickness.[42] Indexing the ED patterns in B and E of Figure 2 reveals the beams are oriented down the [001] and [011] zone axes, respectively. The lattice spacings and crystal symmetry determined by simulating the observed ED patterns match those of mendipite. The only noticeable difference between measured

and simulated ED patterns is the appearance of forbidden diffraction spots. The ED pattern from the [010]-oriented nanowire shows (010) and (030) diffraction spots, which are forbidden, and the [013]-oriented nanobelts show forbidden (300) and (500) diffraction spots. Most likely these forbidden spots appear as a result of kinematic breaks in the crystal lattice symmetry such as monatomic steps along the nanocrystal surface.[43−45]

The belt-like structure and observed crystallographic orientations mirror the bulk crystal structure of mendipite.[46] Figure 3 shows an atomic model of a ⟨010⟩-oriented nanobelt. Mendipite consists of linked [O$_2$Pb$_3$] chains surrounded by Cl$^-$ ions, as

---

(42) Reflections for the (200) lattice plane at 6.21 Å and (400) lattice plane at 3.08 Å are present 90° from the {020} reflections and are also exactly 90° from the [001] zone axis. The orientation of the {020} and {200} reflections with respect to the [001] zone axis indicates that this belt grows in the [010] direction with the width and thickness of the belt oriented in the [100] and [001] directions, respectively.

(43) Gibson, J. M.; Lanzerotti, M. Y.; Elser, V. *Appl. Phys. Lett.* **1989**, *55*, 1394−1396.
(44) Lynch, D. F. *Acta Crystallogr.* **1971**, *A27*, 399−407.
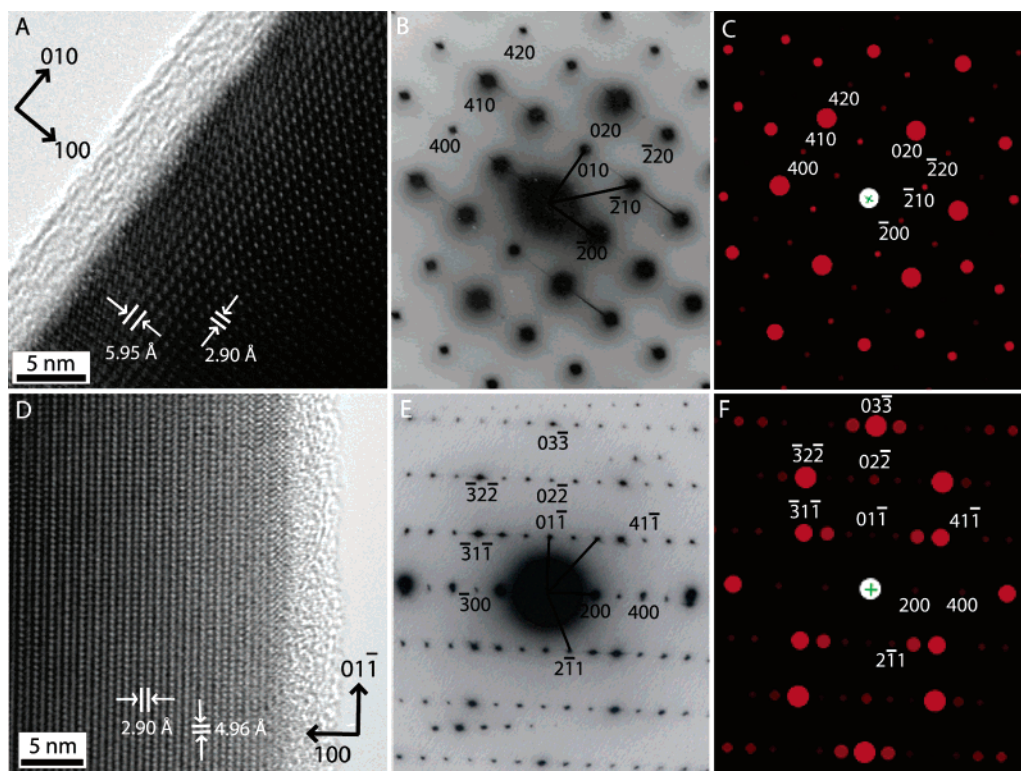(45) Castaño, V.; Gómez, A.; Yacaman, M. J. *Surf. Sci.* **1984**, *146*, L587− L592.

Figure 2. (A) HRTEM image, (B) selective area electron diffraction pattern, and (C) simulated electron diffraction pattern for a $Pb_3O_2Cl_2$ nanobelt imaged down the [001] pole with a ⟨010⟩ growth direction. (D) HRTEM image, (E) selective area electron diffraction pattern, and (F) simulated electron diffraction pattern for a $Pb_3O_2Cl_2$ nanobelt imaged down the [011] pole, exhibiting a ⟨013⟩ growth direction.[46]
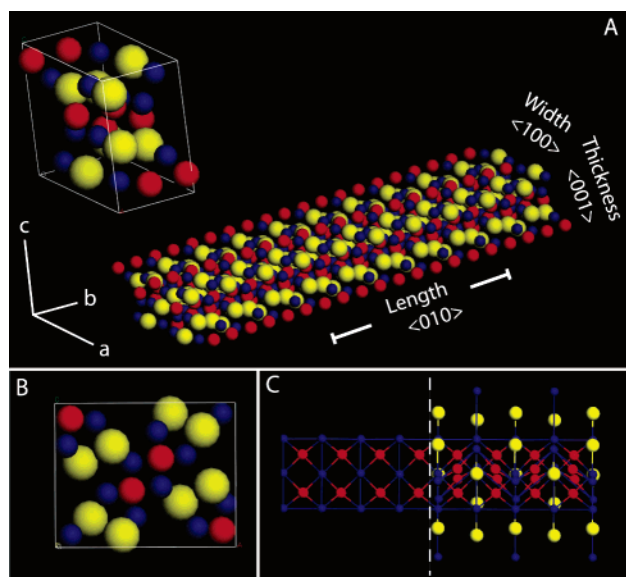
Figure 3. (A) Crystallographic model of a ⟨010⟩ oriented nanobelt. (Inset) Orthorhombic $Pb_3O_2Cl_2$ unit cell (Pb^{2+} ions (blue), O^{2-} ions (red), and Cl^- ions (yellow)). (B) Unit cell viewed from the [010] direction (i.e., the nanobelt cross-section); the linked OPb_4 tetrahedra are visible. (C) Belt viewed down the [$\bar{1}$01] zone axis showing linked [O_2Pb_3] chains stretching down the length of the nanobelt. The peripheral atoms are removed to the left of the dashed line for clarity.

illustrated in Figure 3C.[40] The [O_2Pb_3] chains consist of tetrahedrally coordinated O^{2-} and Pb^{2+} ions that alternate in and out of the plane of the linked chain. The chain in Figure 3C is viewed down the [$\bar{1}$01] zone axis, and would stretch down the length of the nanobelt in the [010] direction. The ⟨010⟩ orientation of the nanobelts accommodates the naturally occurring chains in the crystal.

Nanobelt Birefringence. Bulk $Pb_3O_2Cl_2$ (mendipite) shows relatively strong birefringence. It is a biaxial crystal with direction-dependent refractive indices of 2.27 Å (*a* axis), 2.31 Å (*b* axis), and 2.24 Å (*c* axis) with a maximum difference in refractive index (i.e., birefringence) of 0.07. Despite their narrow dimensions, nanobelt birefringence was easily observed in an optical microscope under polarizers crossed at 90°. Under crossed polarizers, a material that is not birefringent appears dark at all orientations with respect to the polarizer and analyzer angles. A birefringent material changes the incident polarization by splitting linearly polarized light into two perpendicularly polarized components, creating an elliptically polarized beam of light with a component capable of passing through the analyzing filter.[47] When the incident light beam is vibrating parallel to only one optical axis, the material appears dark under crossed polarizers because there is no splitting of the beam; this sample orientation is called the position of extinction. As the sample rotates away from the position of extinction, splitting of the beam occurs, and the sample appears in the microscope. The image is brightest when the polarization angle is 45° from the crossed polarizers. Therefore, the brightness of a birefringent

(46) In the ED patterns, the (0$\bar{1}$1) and (01$\bar{1}$) reflections appear to be oriented towards the length of the nanobelt. However, the [011] is not the growth direction because the angle between the [011] zone axis and the (01$\bar{1}$) lattice plane is 62.8°, ruling out this possibility unless the belt happens to be oriented at an extreme angle of ~27° with respect to the TEM grid. The closest growth direction is [013] (the (01$\bar{3}$) and (013) lattice planes are oriented 87.3° and 92.7° from the [011] zone axis). This is consistent with the image and the ED pattern: the {200} planes appear perpendicular to the growth direction, which meets expectations since the [200] direction is oriented at 90° from both the [011] and [013] directions in the mendipite crystal structure. The visible lattice planes running down the length of the nanobelt match the {013} *d* spacing as well.

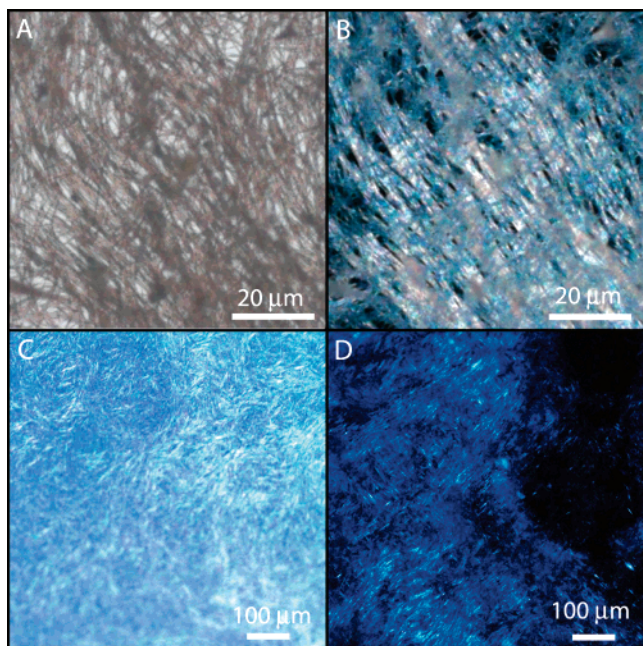(47) For an introductory review of birefringence and polarization microscopy, see http://www.olympusmicro.com/primer/java/polarizedlight/crystal/index.html.

Figure 4. Pb$_3$O$_2$Cl$_2$ nanobelts (A,B) drop-cast onto glass and (C,D) dispersed in chloroform imaged by optical microscopy (A,C) without and (B,D) with crossed polarizers.

material viewed under crossed polarizers relates to the sample orientation with respect to the polarization angle. Figure 4 shows nanobelts deposited on a glass substrate (A and B of Figure 4) and dispersed in chloroform (C and D of Figure 4) imaged with and without crossed polarizers. The nanobelt brightness relates to the nanobelt orientation. Domains of orientational order extend over regions ~200 μm^2 in size, both when deposited on the substrate and in a concentrated dispersion. The range of orientational order on the substrate is consistent with SEM images (Figure 1G).

When drop-cast on substrates from dispersions, the nanobelts tend to rest on their wide axis, the {001} surface. With this nanobelt orientation, the birefringence derives from the refractive index differences in the ⟨010⟩ and ⟨001⟩ directions, and the positions of extinction (when the nanobelt appears dark under crossed polarizers) coincide with nanobelts parallel and perpendicular to the polarization angle. Figure 5 shows two thin bundles of nanobelts deposited at right angles to each other. As expected, the nanobelt appears brightest when their spatial axes are 45° from the polarization angle, and dark at their positions of extinction with either the ⟨010⟩ or ⟨001⟩ directions parallel to the polarization angles. The nanobelts are bright under

the microscope despite the fact that their diameters are much smaller than the wavelength of the incident light.

To obtain a quantitative estimate of the nanobelt birefringence—the difference in refractive index between the ⟨010⟩ and ⟨100⟩ crystallographic directions—a Red 1 compensator was inserted to determine the optical path difference OPD, of the nanobelts. The OPD relates to the sample thickness d, and the refractive indices of the slow and fast directions, n_s and n_f, (i.e., the birefringence):

$$\text{OPD} = d|n_s - n_f| \tag{1}$$

The slow axis of the compensator was oriented at 45° to the polarization angle (NE–SW direction). The compensator is a birefringent material that adds an OPD of 550 nm to the two incident rays of polarized light. When the slow axis ([010] direction) of the nanobelts was oriented parallel to the compensator (Figure 6A), the nanobelt bundle appeared to be a blue color. Using a Michel Lévy chart, the total OPD of the compensator and nanobelt bundle was found to ~650 nm.[48] In this orientation, the OPDs of the nanobelt bundle and compensator add, giving an OPD of ~100 nm. The nanobelts turned reddish-orange when rotated 90° (Figure 6B). From the color, the OPD determined from a Michel Lévy chart is 450 nm. In this orientation the nanobelt and compensator OPDs subtract, and the OPD is again ~100 nm. The measurements reveal that the slow optical axis is the [010] direction—down the length of the belts—as expected from bulk refractive index values. The thickness of the nanobelt bundle imaged under crossed polarizers was then measured using noncontact AFM and found to be 68 nm, as shown in Figure 6, C and D. From eq 1, the birefringence is found to be ~1.5, which is 20 times larger than the bulk birefringence of 0.07 for mendipite.

The OPD estimated from interference colors using the Michel Lévy chart does not provide a high degree of accuracy because of the uncertainty in determining by eye the wavelength from the observed color. Therefore, we wanted to confirm the very high nanobelt birefringence with a more accurate measurement technique, and used Bräce–Köhler and de Sénarmont methods. We first attempted to use a λ/20 Bräce–Köhler compensator. It was inserted between the sample and the analyzing polarizer at 135° (NW–SE direction)—referred to here as the "0"" orientation with respect to the maximum refractive index of the mica prism within its rotary holder. The nanobelts were imaged using a 656 nm band-pass filter, and a maximum OPD of 32.8 nm could be measured using this configuration. The nanobelts were oriented with their lengths ([010] direction) at 45° (NE–

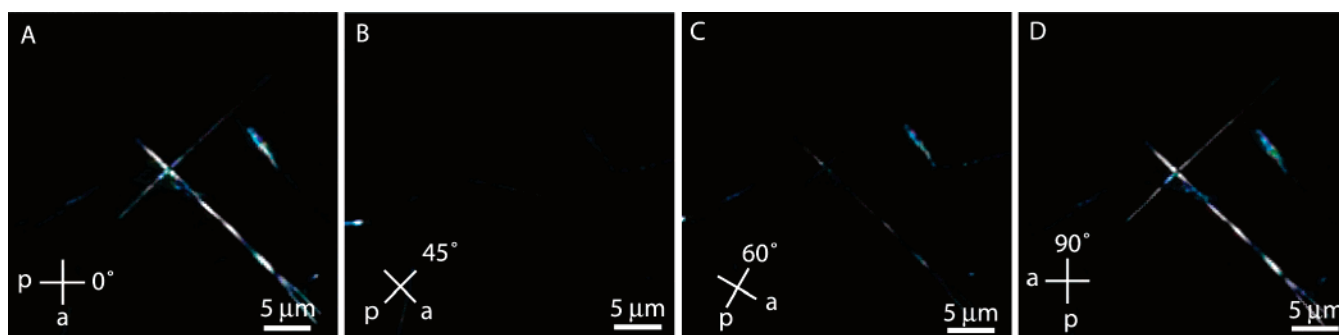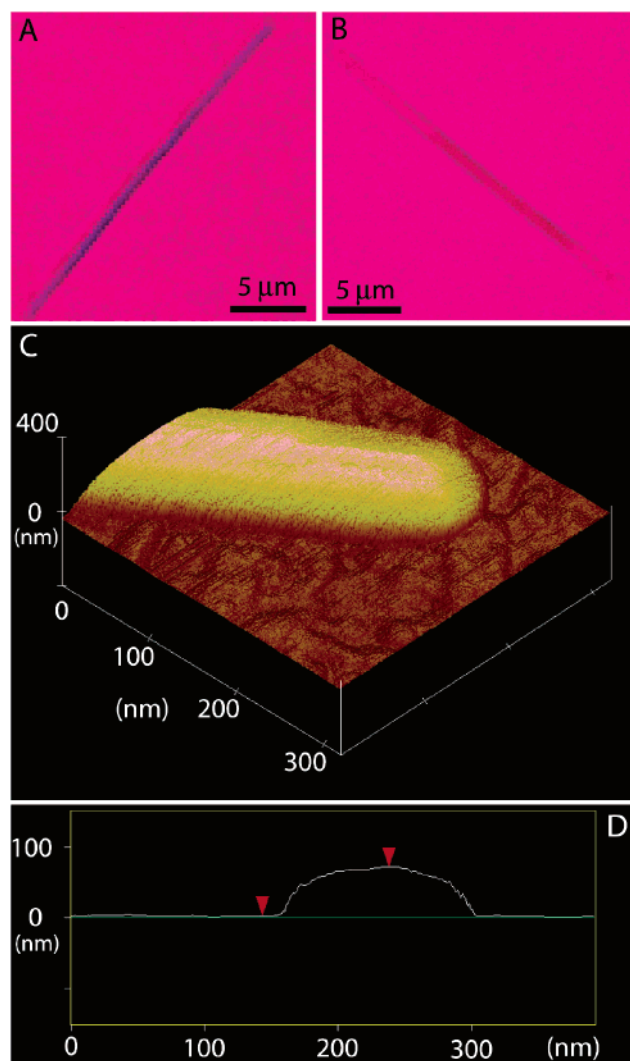**Figure 5.** Two bundles of Pb$_3$O$_2$Cl$_2$ nanobelts on glass imaged by optical microscopy under crossed polarizers at different orientations with respect to the filter angles: Polarizing and analyzing filters (p and a, respectively) oriented at (A) 0° and 90°; (B) 45° and 135°; (C) 60° and 150°; and (D) 90° and 180°.

Figure 6. (A) Nanobelt bundle imaged through crossed polarizers with the slow axis (direction of larger refractive index) of the Red 1 compensator oriented parallel to the length of the belts. (B) Same nanobelt bundle rotated 90° with respect to the orientation of the slow axis of the Red 1 compensator demonstrating change in interference colors. (C) Three-dimensional AFM (tapping mode) image and (D) cross sectional height profile of the same nanobelt bundle imaged in (A) and (B). Dimensions of imaged nanobelt bundle are 68 nm in thickness and 130 nm in width.

SW direction) relative to the crossed polarizers and viewed in the microscope: the nanobelt bundle was dark. By rotating the Bräce−Köhler compensator 360°, two maxima in transmitted light occurred at 90° and 270° and one minimum at 180°. Normally, one expects four positions of extinction, and the observation of only two minima indicates that the OPD exceeds 32.8 nm.[49] For this to be true, the OPD must be greater than 32.8 nm. Given the thickness of the nanobelt bundle (68 nm) measured by AFM, this measurement confirms that the birefringence is greater than 0.48.

An accurate measure of the birefringence was made using de Sénarmont compensation with a larger OPD measurement range of a full wavelength (546 nm). The measurement uses 546 nm monochromatic light with a quarter wave plate inserted with its slow axis oriented 45° relative to the polarizer angle.

(48) Neese, W. D. *Introduction to Optical Mineralogy*; Oxford University Press: New York, 1986.
(49) Anonymous. Bräce−Köhler Rotary Mica Compensator Operating Instructions: Publication #G41-515-e; Carl Zeiss: Germany.
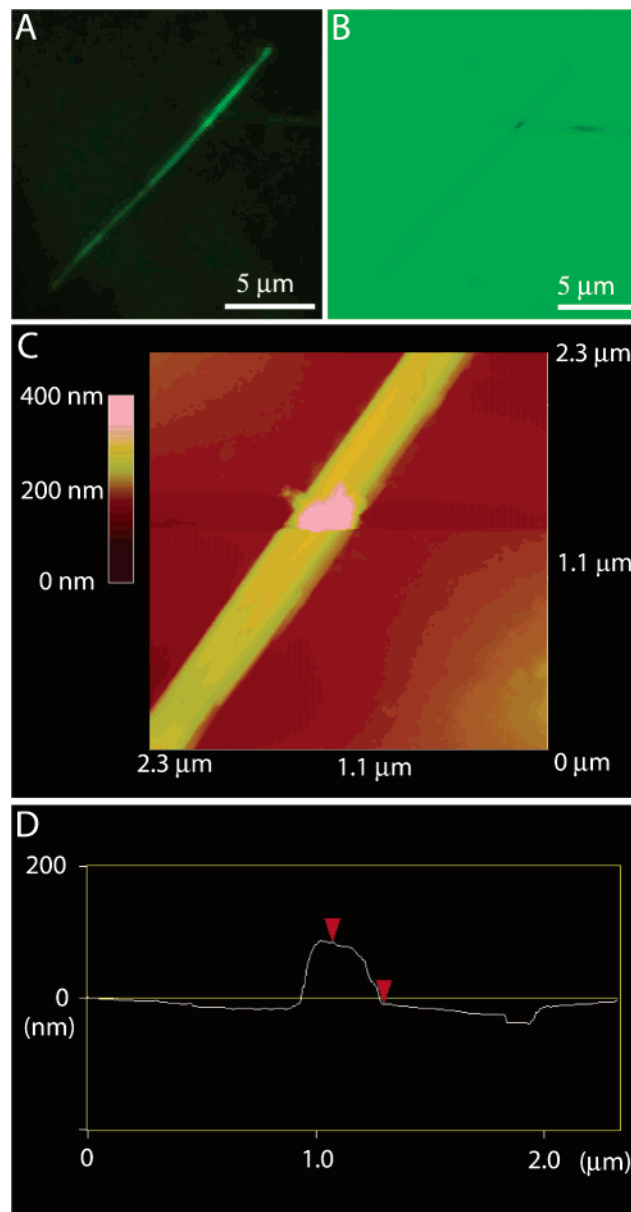
Figure 7. (A) $Pb_3O_2Cl_2$ nanobelt bundle imaged through crossed polarizers with the slow axis (direction of larger refractive index) of the de Sénarmont compensator oriented parallel to the length of the belts with an analyzer angle of 0°. (B) Same nanobelt bundle under de Sénarmont compensation with the analyzer rotated to extinction at 37°. (C) AFM (tapping mode) image and (D) cross sectional profile of the same nanobelts imaged in (A) and (B) used to determine the nanobelts thickness of 103 nm. The larger-than-average thickness and the presence of distinct lateral protrusions along the right side of the structure in (C), along with a corresponding shoulder in the height profile in (D) confirm that this is a bundle of nanobelts being imaged.

Figure 7A shows a nanobelt bundle oriented parallel to the slow axis of the compensator. By rotating the analyzing filter, the nanobelts become dark, reaching a position of extinction at Θ = 37° (Figure 7B). The background changes from black to green as polarized light passes through the analyzing filter at polarization angles <90°. The OPD relates to the angle at extinction Θ:

$$OPD = \frac{\lambda \cdot \Theta}{180°} \qquad (2)$$

Plugging into eq 2, λ = 546 nm and Θ = 37°, the OPD is 112 nm. The thickness for this bundle of nanobelts determined

using noncontact AFM (Figure 7, C,D) is 103 nm, giving a birefringence of 1.1, which is in agreement with the results obtained using interference colors and the Michel Lévy chart, and the Bräce−Köhler method. The average birefringence of three different nanobelt bundles was 1.1 (for bundles 67, 80, and 103 nm thick).

Conclusions

Pb₃O₂Cl₂ nanobelts synthesized using a solventless approach exhibit greatly enhanced birefringence relative to the bulk material. The nanobelts exhibit preferential ⟨010⟩ crystallographic orientations down the nanobelt length, with the width and thickness oriented in the ⟨100⟩ and ⟨001⟩ directions. The birefringence of nanobelt bundles determined using de Sénarmont compensation is 1.1, which is consistent with the very high values observed using the Bräce−Köhler method and interference colors (and a Michel Lévy chart). The largest reported birefringence we know of is 0.43 for the polymer poly-(ethylene 2,6-naphthalene-dicarboxylate) (PEN),[50] with values up to 0.79 extrapolated from experimental results for 100% crystalline PEN.[51] Two of the most birefringent natural minerals are calcite and rutile, which have values of 0.154 and 0.287.[52] The largest reported birefringence of any inorganic material to our knowledge is ∼0.3 for porous Si.[53] Bulk Si is not birefringent, and the wire-like geometry and anisotropic nature of the surfaces seems to give rise to the enhanced birefringence. These previous results, combined with our findings here for Pb₃O₂Cl₂ nanobelts, indicate that nanowires give rise to greatly enhanced birefringence, perhaps even for materials that are not birefringent in the bulk. Furthermore, nanobelts and nanowires with diameters significantly less than the wavelength of visible light can be observed relatively easily under the polarized light microscope due to their strong birefringence, and polarization microscopy may be useful as a general metrology tool for nanowire device fabrication and processing.

Supporting Information Available: Histogram and log-normal distribution of widths for typical nanobelts, and TEM images of nanobelts formed without ethylenediamine. This material is available free of charge via the Internet at http://pubs.acs.org.

JA051956I

(50) Hamza, A. A.; Sokkar, T. Z. N.; El-Bakary, M. A. *J. Opt. A: Pure Appl. Opt.* **2001**, *3*, 421−427.
(51) Cakmak, M.; Kim, J. C. *J. Appl. Polym. Sci.* **1997**, *64*, 729−747.
(52) Physical property data for minerals are located at www.mindat.org.
(53) Kunzner, N.; Kovalev, D.; Diener, J.; Gross, E.; Timoshenko, V. Y.; Polisski, G.; Koch, F. *Opt. Lett.* **2001**, *26*, 1265−1267.